INTERNATIONAL JOURNAL FOR NUMERICAL METHODS IN FLUIDS
Int. J. Numer. Meth. Fluids **28**: 903–915 (1998)

FINITE ELEMENT SIMULATIONS OF INCOMPRESSIBLE FLOW PAST A HEATED/COOLED SPHERE

S MANSOORZADEH, C.C. PAIN, C.R.E. DE OLIVEIRA* AND A.J.H. GODDARD

Applied Modelling and Computation Group, Centre for Environmental Technology, Imperial College of Science, Technology and Medicine, Prince Consort Road, London, SW7 2BP, UK

SUMMARY

This paper reports numerical simulation of the flow past a heated/cooled sphere. A Galerkin finite element method is used to solve the 3D incompressible Boussinesq equations in primitive variable form. Numerical simulations of flow around the sphere for a range of Grashof numbers and moderate Reynolds numbers, were conducted. The drag coefficient for adiabatic flow shows good agreement with standard correlations over the range of the Reynolds numbers investigated. It is shown that the drag can vary considerably with heating of the sphere and that computational fluid dynamics methods can be used to derive constitutive laws for macroscopic momentum and heat exchange in multiphase flow. © 1998 John Wiley & Sons, Ltd.

KEY WORDS: finite elements; incompressible flow; drag coefficient; heat transfer; numerical modelling; solid sphere

1. INTRODUCTION

The flow structure around a sphere has been the subject of extensive research in both experimental and numerical fluid dynamics. The results of flow simulation have a variety of applications in industry, from chemical engineering processes involving the passage of a liquid or gas between solid spheres, to fluidized beds and the field of aerosols.

Moller [1] performed experiments with spheres for the Reynolds number range of $10^3 \leq Re \leq 10^4$, using flow visualization. He reported two different Strouhal numbers in this range of Reynolds number; a high mode and a low mode. Cometta [2] repeated the same experiments, but used a hot wire technique for Reynolds numbers in the range $10^3 \leq Re \leq 4 \times 10^4$. He reported the same high and low modes of vortex shedding. Kim and Durbin [3] also carried out an experiment in the Reynolds number range of $500 \leq Re \leq 6 \times 10^4$. They stated that the two modes of vortex shedding observed are associated with the small scale instability of the separating shear layer and with the large scale instability of the wake. Sakamotto and Hamu [4] experimentally investigated vortex shedding from spheres with Reynolds numbers from 300 to 4×10^4. They demonstrated that at Reynolds number ranging from 8×10^2 to 1.5×10^4, the higher and lower frequency modes of Strouhal number coexist. They also reported that when the Reynolds number exceeds 300 the first instability of the flow starts and hairpin shaped vortices begin to be shed. This pattern of vortex shedding continues up to Reynolds numbers

---

* Correspondence to: Centre for Environmental Technology, Imperial College of Science, Technology and Medicine, Royal School of Mines Building, London SW7 2BP, UK.

CCC 0271–2091/98/160903–13$17.50
© 1998 John Wiley & Sons, Ltd.
Received June 1997
Revised October 1997

of ≈ 800; thereafter hairpin shaped vortices change from laminar to turbulent vortices with alternate fluctuations.

The structure of the flow around a sphere has also been investigated numerically by a number of workers. Rimon and Cheng [5] studied the flow around a sphere for $1 \leq Re \leq 1000$. They used a finite difference method with symmetric axis properties to solve the Navier–Stokes equations. Dennis and Walker [6] also solved the Navier–Stokes equations numerically for axisymmetric flow past a sphere. Aliabadi and Tezduyar [7] solved the 3D equations using the finite element method and parallel processors. They reported that the axisymmetric structure of the wake breaks down at $Re = 400$ and, after passing the transition phase, a periodic solution appears. In the transition phase, vortex shedding appears in the symmetry plane. Wen-Zhong Shen *et al.* [8] used a finite difference method to solve the Navier–Stokes equations in velocity–vorticity form. They studied the structure of flow around a sphere for Reynolds numbers up to 500. For $Re = 40$ and 100, the flow structure was reported to be in a steady state and axisymmetric. A secondary vortex was observed for $Re = 500$.

The flow structure around a sphere in the presence of heat transfer, which has not been addressed in the previous literature, is investigated numerically in this paper. The primitive variable form of the Navier–Stokes equations in 3D, together with the energy and continuity equations, have been solved. A Galerkin finite element method has been used to solve these

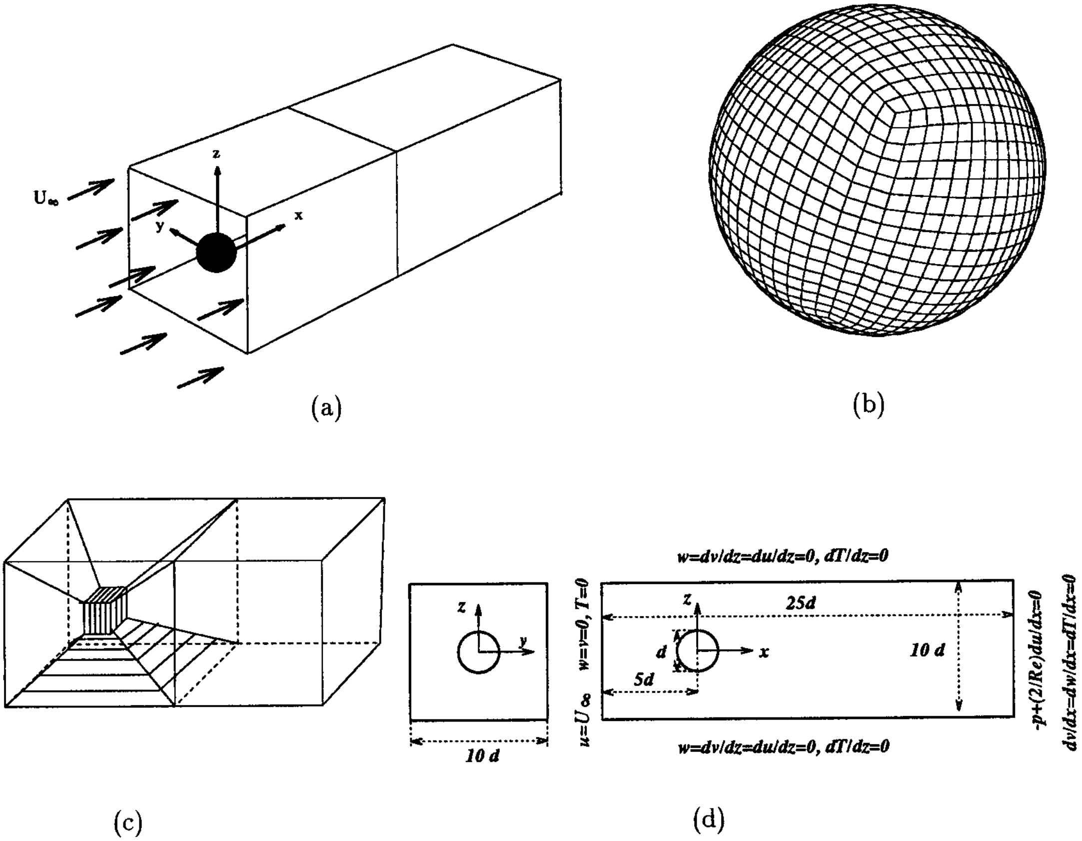

Figure 1. (a) Schematic of the computational domain; (b) mesh structure on the surface of the sphere; (c) the mesh structure comprises seven submeshes, each having a structured connectivity; (d) boundary conditions in the x–z plane. Similar boundary conditions are used in the x–y plane.

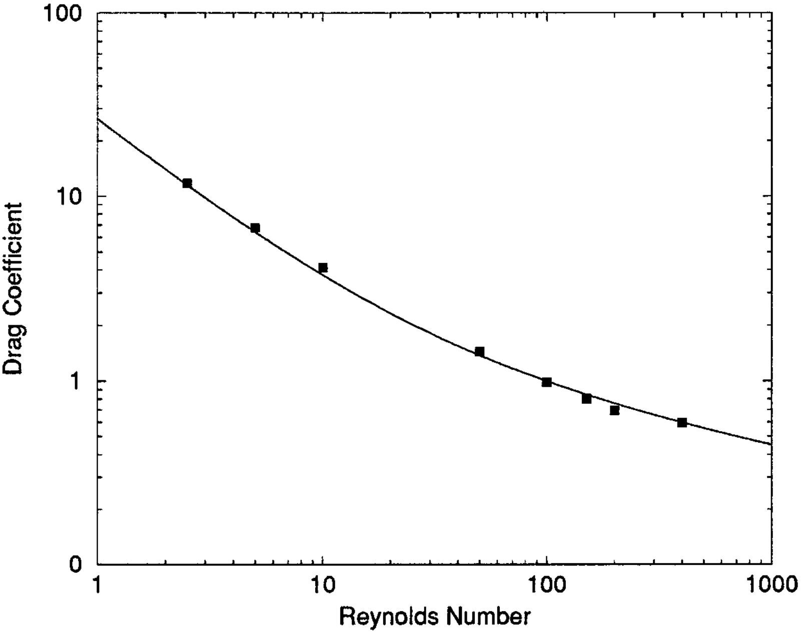

Figure 2. Comparison between the numerically calculated drag coefficients at various Reynolds numbers and experimental data (the continuous line) from Reference [11].

equations. The next section describes the governing equations and the numerical method used to solve them. In Section 3, the numerical results are presented, followed by discussions about the results. Finally, conclusions are drawn in Section 4.

2. GOVERNING EQUATIONS AND NUMERICAL METHODS

Assuming a viscous and incompressible flow, and using a Boussinesq approximation, the Navier–Stokes, energy and continuity equations can be written as

$$\frac{\partial u}{\partial t} + \nabla \cdot (uV) = -\frac{\partial p}{\partial x} + \frac{1}{Re} \nabla^2 u + RiT, \tag{1}$$

$$\frac{\partial v}{\partial t} + \nabla \cdot (vV) = -\frac{\partial p}{\partial y} + \frac{1}{Re} \nabla^2 v, \tag{2}$$

$$\frac{\partial w}{\partial t} + \nabla \cdot (wV) = -\frac{\partial p}{\partial z} + \frac{1}{Re} \nabla^2 w, \tag{3}$$

$$\frac{\partial T}{\partial t} + \nabla \cdot (TV) = \frac{1}{Pe} \nabla^2 T, \tag{4}$$

$$\frac{\partial u}{\partial x} + \frac{\partial v}{\partial y} + \frac{\partial w}{\partial z} = 0, \tag{5}$$

where V is the velocity vector, with u, v and w components in the x-, y- and z-directions respectively, p is the pressure and T is the temperature. Re is the Reynolds number, Gr is the

© 1998 John Wiley & Sons, Ltd.

Grashof number, Pe is the Peclet number, Ri is the Richardson number, and they are defined as

$$Re = \frac{U_\infty d}{v}, \qquad Gr = \frac{g\beta d^3}{v^2}(T_s - T_f), \qquad Pe = \frac{U_\infty d}{\alpha}, \qquad Ri = \frac{Gr}{Re^2},$$

where U_∞ is the characteristic velocity, the inlet velocity in this case, d is the characteristic length, denoting the diameter of the sphere, v is the kinematic viscosity, β is the thermal expansion coefficient, g is the gravity acceleration, α is the thermal diffusivity and $T_s - T_f$ is the temperature difference between a constant sphere surface temperature T_s and a constant inflow temperature T_f.

The non-dimensional inflow temperature T_f and the sphere surface temperature T_s are specified as $T_f = 0$ and $T_s = 1$. A positive Richardson number represents a heated sphere surface in which the buoyancy acts in the opposing direction to the gravitational force. In the same way, a negative Richardson number indicates a cooled sphere surface in which buoyancy and gravity forces have the same directions.

Using the Galerkin discretization method, the discretized Navier–Stokes equations can be written as

$$\hat{M}\left(\frac{V^{n+1} - V^n}{\Delta t}\right) = -KV^{n+\theta} - NV^{n+\theta} + Cp^{n+1}, \tag{6}$$

where $\hat{M}$ is mass matrix, K and N are matrices associated with diffusion and advection terms, and n and θ denote the discretized time level at which velocity and pressure are calculated. A

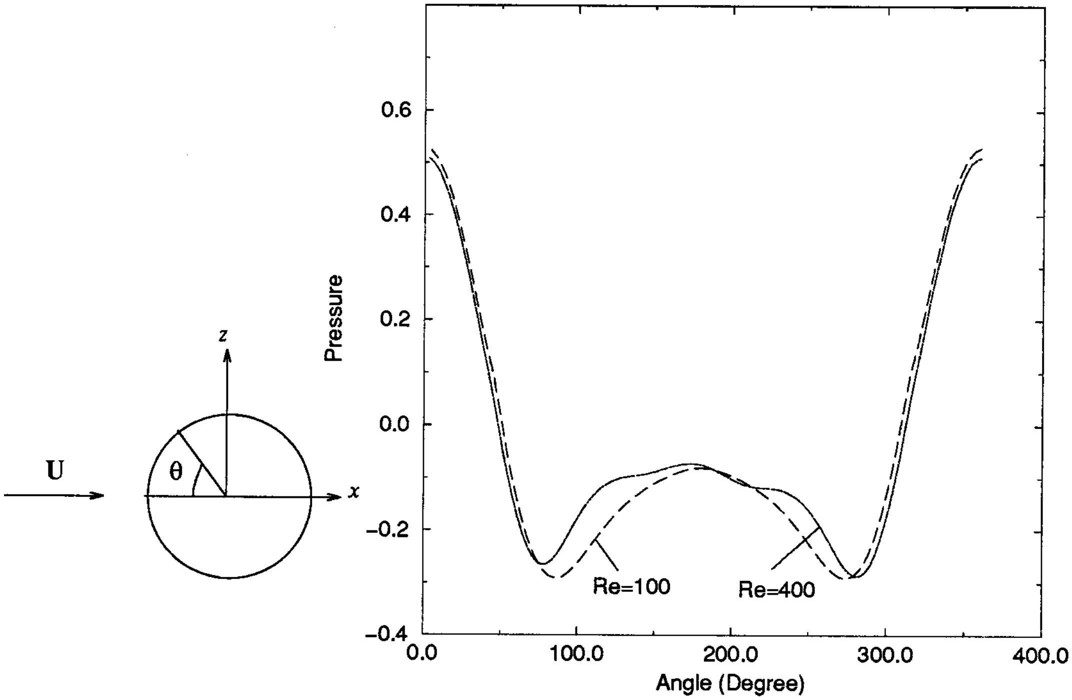

Figure 3. Pressure distribution at $t = 93.4$ for $Re = 100$ and 400 on the x–z plane for $y = 0$. At $Re = 400$ the symmetry is broken.

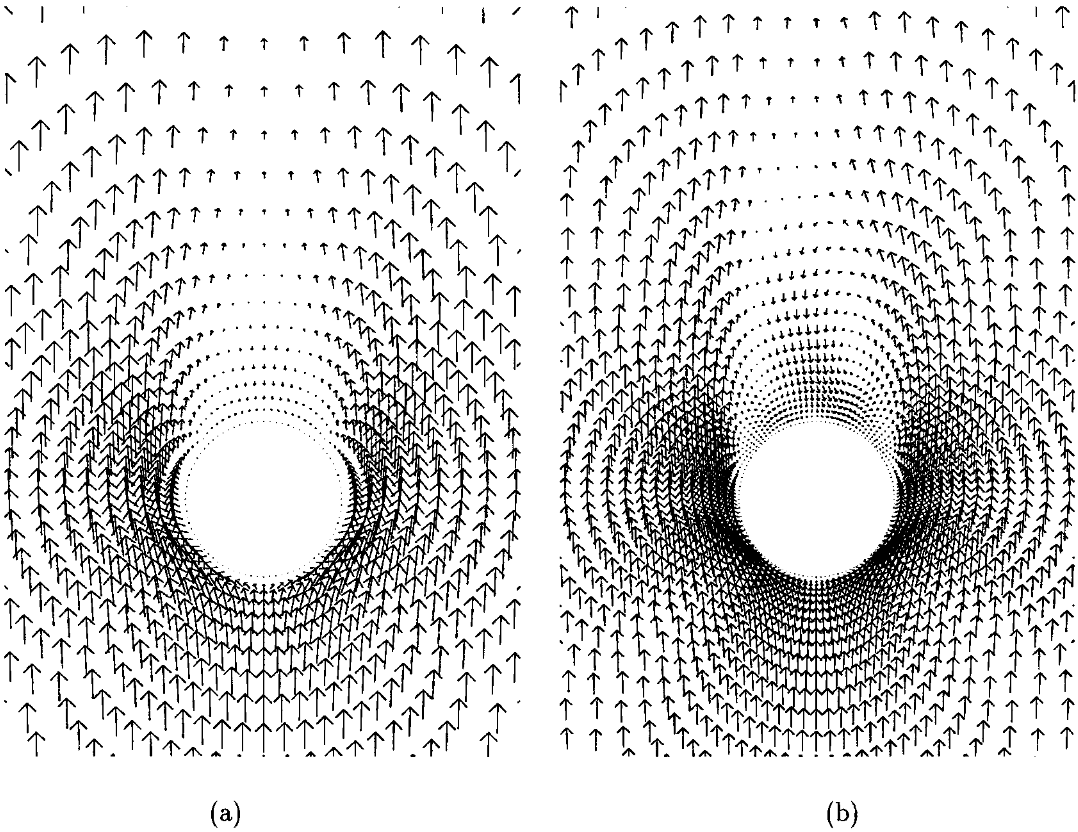

Figure 4. Velocity vectors without heat transfer at (a) $Re = 100$, and (b) $Re = 400$, at time $t = 93.4$. At $Re = 400$, the symmetry of the flow breaks down.

Crank–Nicolson time discretization method, $\theta = 1/2$, is used with the Galerkin finite element, because this minimizes the dissipative effects on the solution.

It is assumed that V^{n+1} and p^{n+1} satisfy both this equation as well as the continuity equation. If V_* and p_* are the velocity and pressure fields that satisfy this equation, but not necessarily the continuity equation, then

$$\hat{M}\left(\frac{V_*^{n+1} - V^n}{\Delta t}\right) = -KV^{n+\theta} - NV^{n+\theta} + Cp_*^{n+1}. \tag{7}$$

Subtracting Equation (7) from Equation (6) gives

$$\hat{M}\left(\frac{V^{n+1} - V_*^{n+1}}{\Delta t}\right) = C(p^{n+1} - p_*^{n+1}). \tag{8}$$

Pre-multiplying this equation by $C^T M_{\mathrm{L}}^{-1}$ gives

$$C^T M_{\mathrm{L}}^{-1} \hat{M}\left(\frac{V^{n+1} - V_*^{n+1}}{\Delta t}\right) = C^T M_{\mathrm{L}}^{-1} C(p^{n+1} - p_*^{n+1}). \tag{9}$$

Introducing a modified continuity equation as $C^T M_{\mathrm{L}}{}^{-1} \hat{M} V^{n+1} = 0$ in the above equation, results in

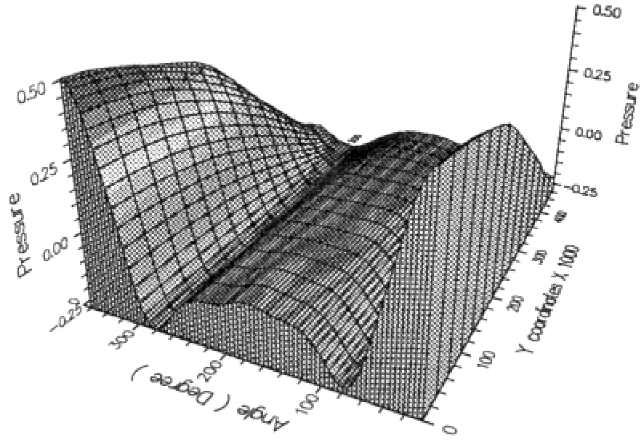

Figure 5. Pressure distribution at various y sections for the adiabatic case at $Re=400$ for time $t=93.4$.

$$\frac{-C^{T}M_{\mathrm{L}}^{-1}\hat{M}V_{*}^{n+1}}{\Delta t}=C^{T}M_{\mathrm{L}}^{-1}C\Delta p, \tag{10}$$

where $\Delta p=(p^{n+1}-p_{*}^{n+1})$.

A projection method was used to solve the Navier–Stokes equations. In this method, initializing with $p_{*}^{n+1}=p_{*}^{n}$, Equation (7) is solved for V_{*}^{n+1}. Then V_{*}^{n+1} is used in Equation (10) to solve for the pressure. Finally, Equation (8) is solved for V^{n+1}. The new pressure can be calculated by adding Δp to the previous p_{*}, i.e.

$$p_{*}(\text{new})=p_{*}(\text{old})+\Delta p, \tag{11}$$

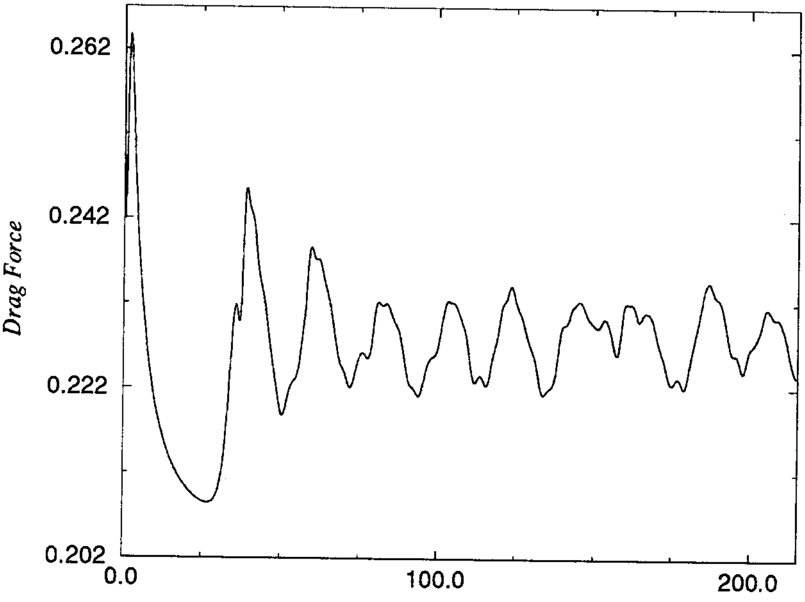

Figure 6. Variation of the force exerted on the sphere in the direction of flow, x-direction.

© 1998 John Wiley & Sons, Ltd.

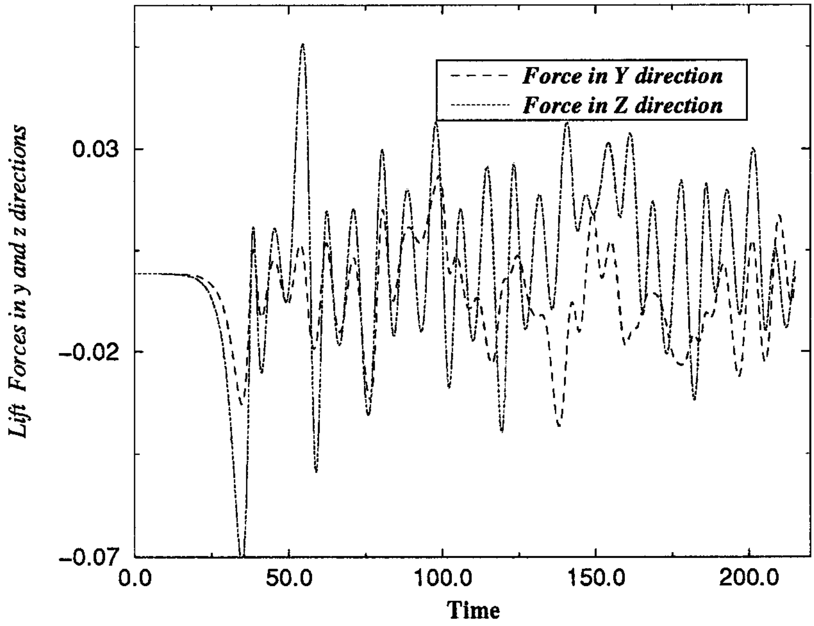

Figure 7. Variation of the forces exerted on the sphere in the y- and z-directions for the adiabatic case with $Re = 400$.

and the process is repeated until convergence. Often, however, only a single iteration is used per time step, e.g. Gresho *et al.* [9]. In solving Equation (10), if instead of both M_{L}^{-1} and $\hat{M}$, a distributed mass matrix M is used, then the method is called the consistent mass matrix method. This method is accurate but expensive, because in this case the inverse mass matrix may be dense, making $C^{T}M^{-1}C$ dense and difficult to invert.

If a lumped mass matrix, M_{L}, is used for $\hat{M}$, then the method is termed the lumped mass matrix method. Calculating M_{L}^{-1} is easy and cheap, but the accuracy will be reduced.

If a distributed mass matrix is used for $\hat{M}$, and a lumped mass matrix used in Equation (10), the method is termed a mixed mass method. This method is more accurate than the lumped mass matrix method and cheaper than the consistent mass matrix method. The mixed mass method of Gresho and Chan [9] alters the pressure which detracts from the accuracy of the computed pressure and drag around the sphere. The discretized pressure term in this approach is altered to $M_{\mathrm{L}}^{-1}M_{C}CP$. Due to problems in calculating the drag using the mixed mass method, the lumped mass matrix method was used.

The drag coefficient can be calculated according to the equation

$$C_{\mathrm{D}} = \frac{F_X}{1/2\rho U^2 A}, \tag{12}$$

in which A is the projection area of the sphere and

$$F_X = \int \mu\left(\frac{\partial v}{\partial x} + \frac{\partial u}{\partial y}\right)n_y + \mu\left(\frac{\partial u}{\partial z} + \frac{\partial w}{\partial x}\right)n_z + 2\mu\frac{\partial u}{\partial x}n_x - pn_x\Bigg)\,\mathrm{d}A. \tag{13}$$

Similar expressions can be used for forces in the Y- and Z-directions. A variety of drag correlations for the flow past a sphere exist; the present results are compared with the correlation [10]

$$C_{\mathrm{D}} = \frac{24}{Re_p}\,(1 + 0.1Re_p^{0.75}).$$

© 1998 John Wiley & Sons, Ltd.

3. NUMERICAL RESULTS AND DISCUSIONS

The grid structure on the surface of the sphere and the computational domain used in this study are illustrated in Figure 1. Figure 1(c) shows that the structure of the mesh consists of seven submeshes, each having a structured connectivity. Element sizes around the sphere decrease exponentially towards the sphere. Boundary conditions used in this simulation are shown in Figure 1(d).

First, the accuracy of the code for the adiabatic case at Reynolds numbers between 2 and 500 are checked. The drag coefficients are time averaged for the larger Reynolds numbers. In Figure 2, the calculated drag coefficients and the experimental data from Reference [10] are compared. Over this range of Reynolds numbers, the calculated drag coefficients show good agreement with the experimental data. Various grid sizes are used for the simulations. At lower Reynolds numbers (<400), 58 000 and at higher Reynolds numbers (≥ 400), about 160 000 hexahedral elements are used. All the elements have tri-linear variations of velocity and constant pressure across each element. A dimensionless time step of 0.05 is used.

Pressure distributions for the adiabatic case show that, at low Reynolds numbers, the flow is axisymmetric and at a Reynolds numbers ≈ 400, the symmetry is broken. Figure 3 shows the pressure distribution on the x–z plane through the centre of the sphere for $Re = 100$ and 400. The velocity vectors for these cases are shown in Figure 4. As can be seen from these figures, the velocity vectors and pressure distribution are not symmetric for $Re = 400$. The pressure distribution at various y sections is shown in Figure 5. Variation of the force exerted on the sphere in the direction of the flow, obtained by Equation (13), is shown in Figure 6. The lift forces, forces in the y- and z-directions resulting from asymmetry of the flow, are also shown in Figure 7. The calculated drag history is consistent with the results of Reference [7].

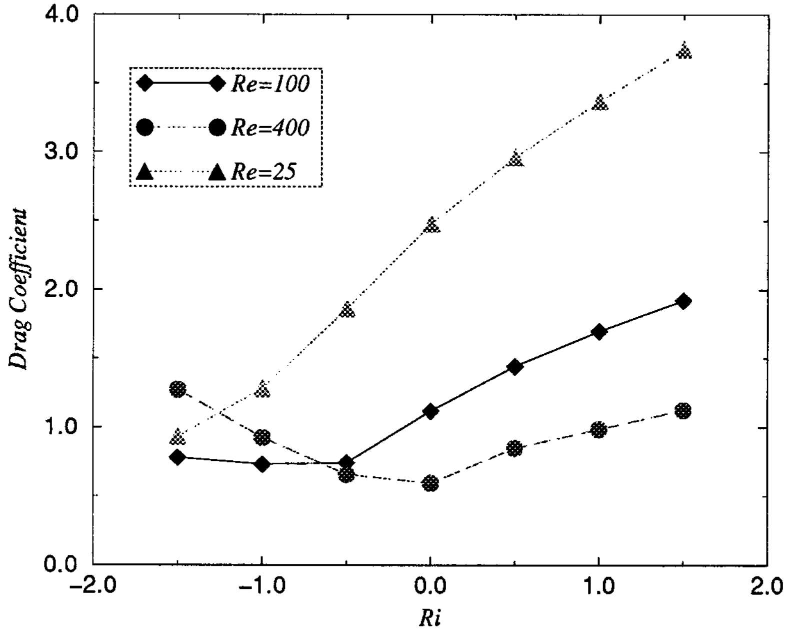

Figure 8. Variation of the drag coefficient C_D as a function of Richardson number for $Re = 100$ and 400.

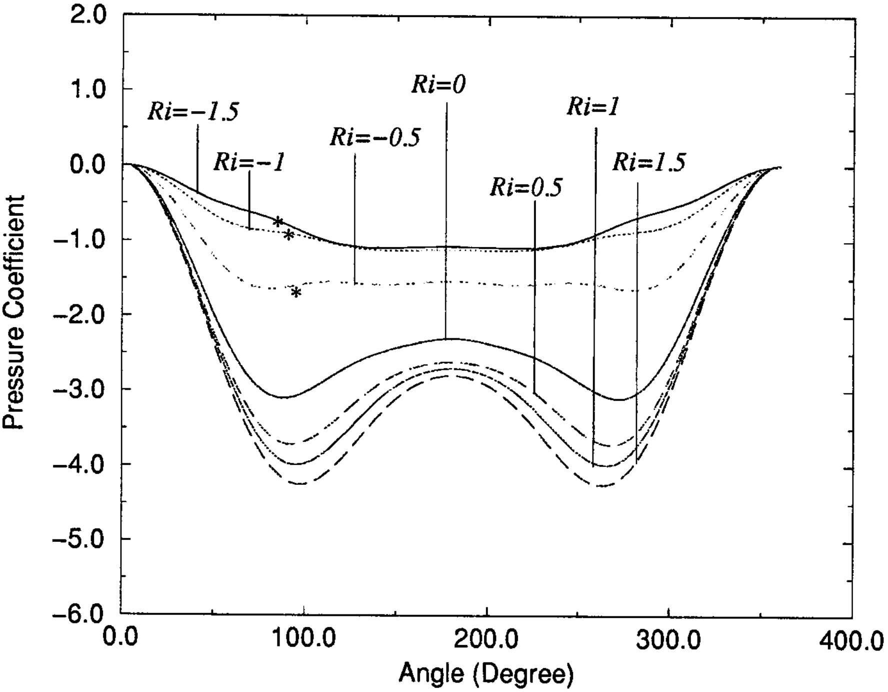

Figure 9. Pressure coefficient C_P, defined as $C_p = P - P_{\theta=0}/(1/2\rho U_\infty^2)$ for various Richardson numbers at $Re = 100$. Upon increasing the Richardson number, the pressure drop between upstream and downstream of the flow increases. By decreasing the Richardson number from -0.5 to -1.5, the separation points, indicated by *, move upstream.

Numerical simulation of a cooled/heated sphere started at a Reynolds number of 100. The Grashof number was varied between -15000 and 15000, corresponding to Richardson numbers of -1.5 to 1.5. A Peclet number of 70.6 was used for the simulations (corresponding to $Pr = 0.706$ for air at $T = 27°\text{C}$, a velocity of 0.17 m s^{-1}, $\Delta T = 130°\text{C}$ and a sphere with diameter of 1 cm).

Figure 8 shows the variation of drag coefficients as a function of Richardson number. The simulations show that, in this range of Richardson number and at a Reynolds number $Re = 100$, increasing the Richardson number increases the drag coefficient. The reason for this behaviour is that, upon increasing the Richardson number from $Ri = 0.0$ to 1.5 and hence increasing the buoyancy force exerted from the cold flow towards the hot sphere, the velocity downstream and next to the surface of the sphere increases. Therefore, the pressure decreases (Bernoulli equation). As a result, the pressure difference between the forward portion of the sphere and behind the sphere increases, as shown in Figure 9. By increasing this pressure difference, which is the main contributor to drag (drag due to pressure is called form drag), the drag coefficient increases. In contrast, upon decreasing the Richardson number from 0.0 to -1, the pressure difference between the side facing the flow and the opposite side of the sphere decreases, therefore the drag coefficient decreases. Further decreases in the Richardson number, from -1 to -1.5, do not decrease the pressure drop appreciably, therefore the drag coefficient is slightly increased. Impulsive initializing of the simulation results in a high pressure drop and a large drag force; therefore the main part of the drag, at the beginning of the simulation, is due to form drag.

© 1998 John Wiley & Sons, Ltd.

In the cooled sphere case, upon decreasing the Richardson number from 0.0 to -1.5, the buoyancy force exerted from the sphere side towards the hot flow causes the flow to separate. In this case, the flow takes a long time to achieve a steady state. For example at $Ri = -1.5$, achieving a steady state takes 80 dimensionless time units, d/U_∞, while for $Ri = 1.5$ the system becomes steady after only 12 time units. The temperature contours for $Ri = -1.5$ and $+1.5$ are shown in Figure 10. The corresponding velocity vectors for these cases are shown in Figure 11. As shown in Figure 11, upon decreasing the Richardson number from $Ri = 1.5$ to -1.5, the flow is separated at a θ value of $\approx 85°$ and the direction of the flow downstream of the sphere is reversed, causing a more uniform pressure distribution (Figure 9), and reducing the drag coefficient. Convergence tests carried out for the simulations showed that the separation points are not sensitive to the meshes used for the calculations.

Heat transfer was also calculated at various Richardson numbers. The following relation was used to calculate the heat transfer:

$$Q = \int_\Gamma k \frac{\partial T}{\partial n}\, d\Gamma,$$

where Q is the heat transfer, k is the thermal conductivity and n is the unit vector normal to the surface Γ of the sphere. Figure 12 shows the variation of heat transfer, normalized with respect to the heat transfer at $Ri = 0.0$ and $Re = 100$, as a function of Richardson number. The non-dimensionalized heat transfer at $Ri = 0.0$ and $Re = 100$ is 0.484×10^{-4}. This figure shows

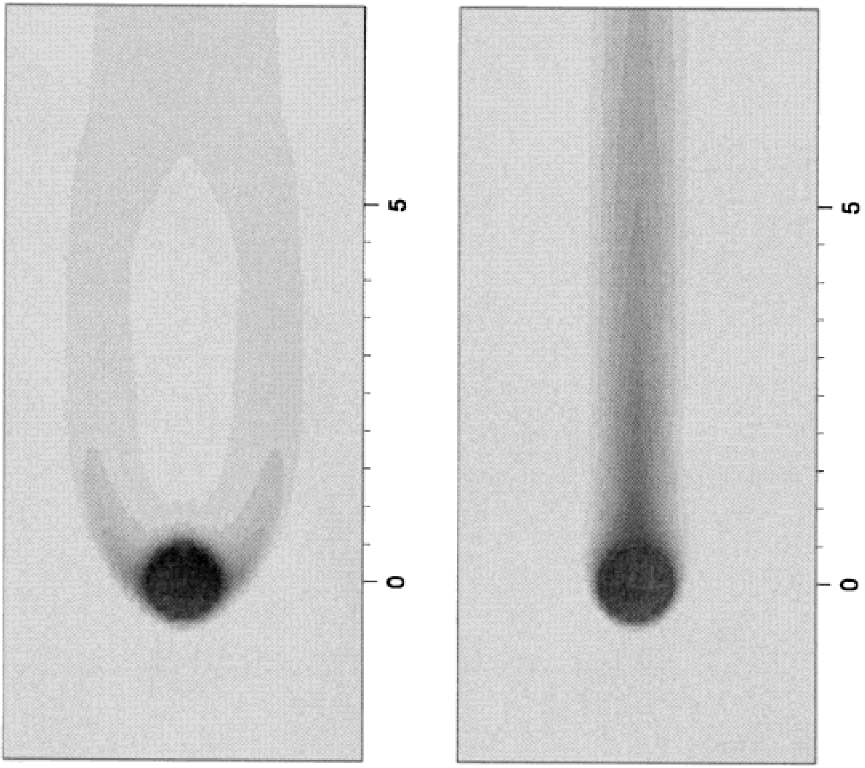

(a) (b)

Figure 10. Temperature contours for (a) $Ri = -1.5$, and (b) $Ri = +1.5$ at $Re = 100$ for time $t = 91$.

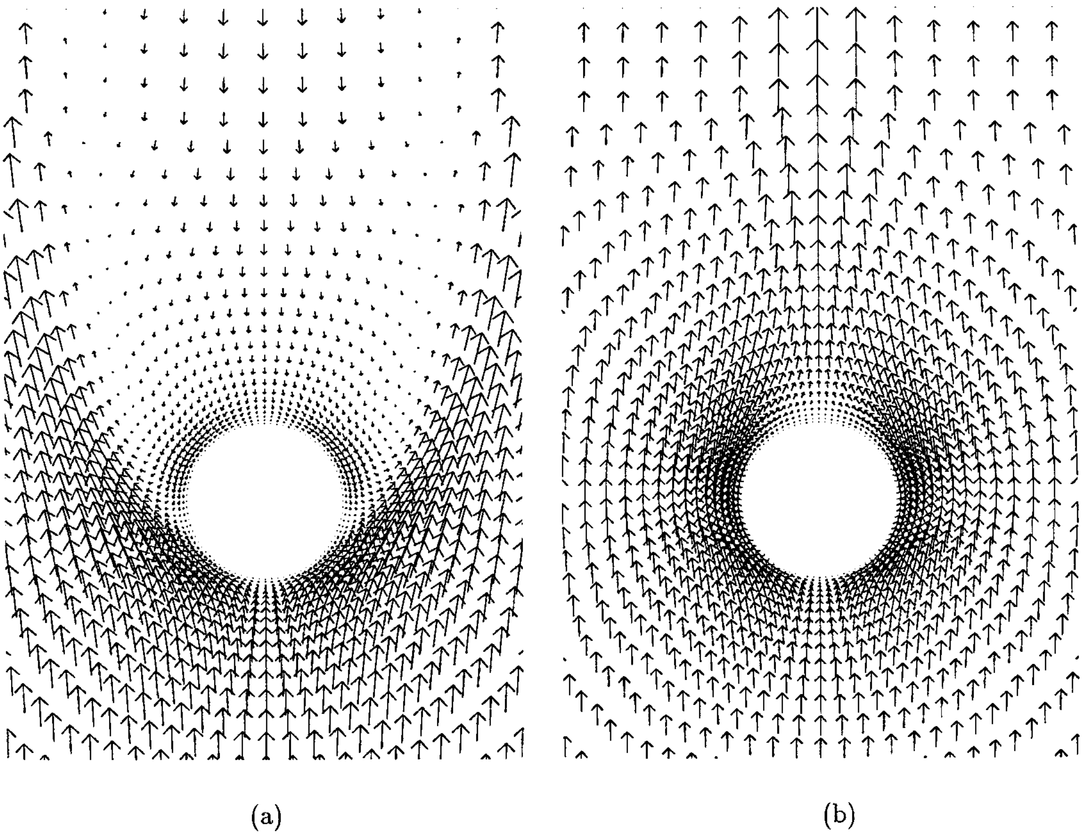

Figure 11. Velocity vectors for (a) $Ri = -1.5$, and (b) $Ri = +1.5$ at $Re = 100$ and $t = 91$. At $Ri = -1.5$ the direction of the flow in the downstream of the sphere is reversed.

that by introducing the buoyancy force, $Ri \neq 0$, the heat transfer increases. The same calculation is repeated for $Re = 400$ and the Richardson number varied between -1.5 and 1.5. As Figure 8 shows, for this Reynolds number, the drag coefficient increases as the Richardson number increases from 0 to 1.5. The simulations showed that by decreasing the Richardson number from 0 to -1.5, the separation points on the sphere move upstream. At a certain Richardson number ($\approx Ri = 0$ for $Re = 400$) further reduction of the Richardson number does not decrease the drag coefficient. Since the separation on the sphere occurs more upstream at $Ri = -1.5$ than at $Ri = -1$ the resulting flow in the former case sees the sphere as a 'bluffer' object than in the latter case, causing the drag coefficient to increase. This situation can be seen in the velocity vectors in Figure 13.

The upstream movement of the separation point, for decreasing the Richardson number, is much reduced if a Reynolds number of 25 is used instead of 400. Therefore, decreasing the Richardson number from 1.5 to -1.5 decreases the drag coefficient continuously. The data shown in Figures 8 and 12 can be used to establish the constitutive relations for many non-adiabatic multiphase modelling applications.

Applying a periodic boundary condition in order to model a uniform distribution of spheres will be the subject of future study. A further step is to allow spheres to move freely, which has already been performed for 2D simulation [11].

© 1998 John Wiley & Sons, Ltd.

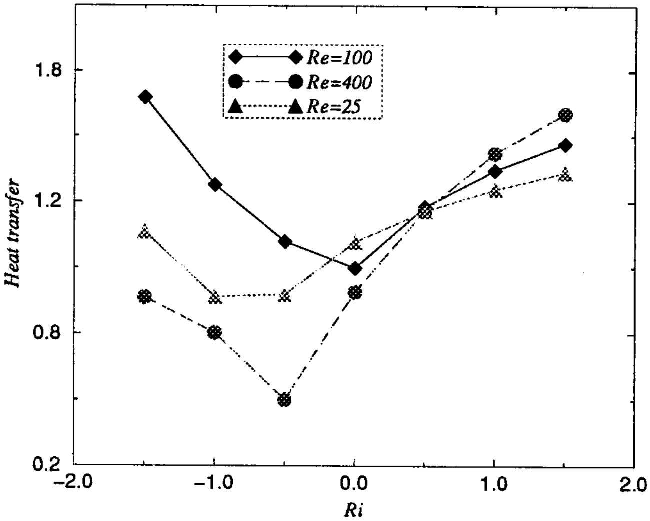

Figure 12. Variation of heat transfer as a function of the Richardson number at various Reynolds numbers. The heat transfer is normalized with respect to heat transfer at $Ri = 0.0$ and $Re = 100$. The non-dimensionalized heat transfer at $Ri = 0.0$ and $Re = 100$ is 0.484×10^{-4}.

4. CONCLUSIONS

The flow structure around a heated/cooled sphere has been simulated using a three-dimensional finite element method. A variety of applications in industry, such as fluidized beds and chemical processes involving the passage of a fluid between solid spheres in the presence of heat transfer, can be treated with this modelling approach.

Drag coefficients calculated from the simulation for the unheated sphere showed good agreement with the correlation presented in [10]. The results showed that at $Re = 400$, symmetry of the flow is broken. A set of calculations has been carried out for three different

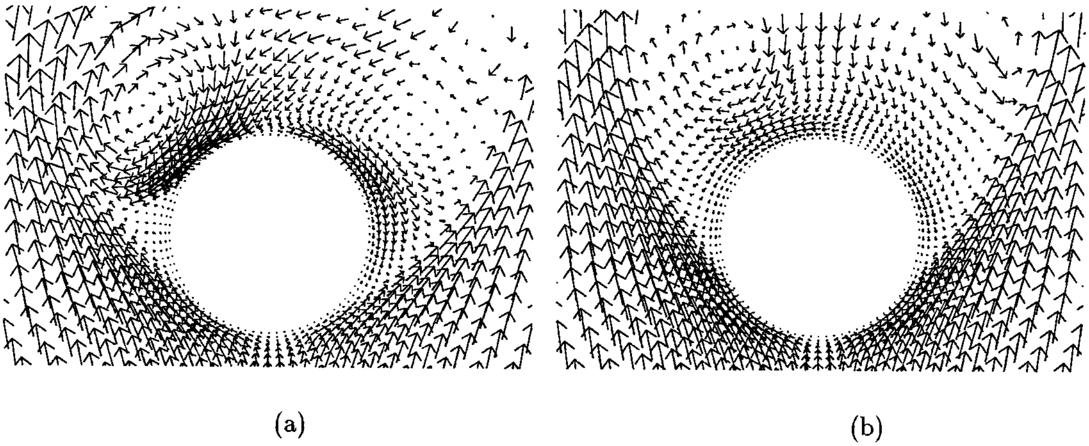

Figure 13. Velocity vectors for (a) $Ri = -1.5$, and (b) $Ri = -1$ at $Re = 400$. As the Richardson number decreases from -1 to -1.5 the separation point moves upstream.

© 1998 John Wiley & Sons, Ltd.

Reynolds numbers, i.e. $Re = 25$, 100 and 400. The Richardson number was varied between -1.5 and 1.5. In all cases, as the Richardson number increased from 0 to a positive number, the pressure difference across the sphere increased, causing the drag coefficient to increase. For example, for $Re = 100$, as the Richardson number varied in the range of 0–1.5, the simulation showed an increase of $\approx 70\%$ in the drag coefficient. The simulation also showed that the separation points move upstream when the Richardson number decreases. For low Reynolds numbers, e.g. $Re = 25$, on reducing the Richardson number from 0 to -1.5, the pressure difference decreases and therefore the drag coefficient decreases. For higher Reynolds numbers, however, e.g. $Re = 400$, the effect of movement of the separation points becomes more pronounced upon decreasing the Richardson number from 0 to -1.5, causing the 'shape' of the object as seen by the flow to change and the drag coefficient to increase.

REFERENCES

1. W. Moller, 'Experimentelle Untersuchung zur Hydromechanick der Hugel', *Phys. Z*, **35**, 57–80 (1938).
2. C. Commetta, 'An investigation of the unsteady flow pattern in the wake of cylinder and spheres using a hot wire probe', *Tech Rep WT-21*, Division of Engineering, Brown University, 1957.
3. K.J. Kim and P.A. Durbin, 'Observation of the frequencies in a sphere wake and drag increase by acoustic excitation', *Phys. Fluids*, **31**, 3260–3265 (1961).
4. H. Sakamotto and H. Hamu, 'A study on vortex shedding from spheres in a uniform flow', *J. Fluids Eng.*, **112**, 386–392 (1990).
5. Y. Rimon and S.I. Cheng, 'Numerical solution of a uniform flow over a sphere at intermediate Reynolds Numbers', *Phys. Fluids*, **12**, 949–959 (1969).
6. S.C.R. Dennis and J.D.A. Walker, 'Calculation of unsteady flow past a sphere at low and moderate Reynolds numbers', *J. Fluid Mech.*, **48**, 771–789 (1971).
7. S.K. Aliabadi and T.E. Tezduyar, 'Parallel fluid dynamics computations in aerospace applications', *Int. J. Numer. Methods Fluids*, **21**, 783–805 (1995).
8. Wen-Zhong Shen and Ta-Phuoc Loc, 'Numerical method for unsteady 3D Navier–Stokes equations in velocity–vorticity form', *Comput. Fluids*, **26**, 193–216 (1997).
9. P.M. Gresho and S.T. Chan, 'On the theory of semi-implicit projection methods for viscous incompressible flow and its implication via a finite element method that also introduces a nearly consistent mass matrix', *Int. J. Numer. Methods Fluids*, **11**, 621–659 (1990).
10. M. Ishi and N. Zuber, 'Drag coefficient and relative velocity in bubbly, droplet or particulate flows', *AIChE J.*, **25**, 843–855 (1979).
11. H.H. Hu, 'Direct simulation of solid–liquid mixtures', *Int. J. Multiphase Flow*, **22**, 335–352 (1996).

© 1998 John Wiley & Sons, Ltd.